Extreme Mechanics Letters 56 (2022) 101893

Contents lists available at ScienceDirect

Extreme Mechanics Letters

journal homepage: www.elsevier.com/locate/eml

Mechanical properties of phenine nanotubes

Bruno Faria [a,*], Nuno Silvestre [b]

[a] IPC-Institute for Polymers and Composites, Polymer Engineering Department, University of Minho, Guimarães, Portugal
[b] IDMEC, Department of Mechanical Engineering, Instituto Superior Técnico, Universidade de Lisboa, Portugal

ARTICLE INFO

Article history:
Received 23 May 2022
Received in revised form 14 August 2022
Accepted 8 September 2022
Available online 16 September 2022

Keywords:
Carbon allotropes
Mechanical properties
Phenine nanotubes
Molecular dynamics
Buckling

ABSTRACT

Phenine Nanotubes (PhNT) are cylinder-shaped molecules synthetized from 1,3,5-trisubstituted benzene ring building blocks that can form tubular segments of different sizes. Small nanotube segments have been recently synthetized, and efforts are being made to increase the nanotubes' length by adding more "phenine" units. To the authors' best knowledge, a complete characterization of the mechanical properties of these nanotubes has not yet been accomplished. In this work, Reax and AIREBO forcefields were used to model armchair and zigzag PhNTs and Molecular Dynamics simulations were employed to determine their mechanical properties for tensile, compressive, bending and twisting loadings. It was found that PhNTs have a much lower Young's modulus (about 30%) and tensile strengths (about 45%) than carbon nanotubes (CNTs), but can endure longer tensile strains without breaking apart. Although possessing a lower bending and twisting stiffness than CNTs, PhNT have highly flexible sidewalls due to their superior porosity, and therefore can withstand higher angles of twist and angles of bend without breaking bonds. This extra flexibility; extended porosity; possibility for heteroatom doping and reasonable strength, make PhNTs very promising candidates for a wide range of applications, such as sensing, ionic transistors or molecular sieving. Finally, a brief study on the application of elastic continuum shell formulas to predict the critical stress (compression), critical moment (bending) and critical torque (twisting) is also presented.

1. Introduction

The bottom-up design of carbon-based nanotubes with tailored pores in their sidewalls has been a major focus of research. Since the discovery of carbon nanotubes, CNTs, [1], the introduction of pores with different sizes in the nanotube's graphenic walls has been attempted, either through the existence of atomic vacancies [2–4] or by the modification of the nanotube's carbon lattice [5]. The insertion of pores in CNTs enables their use in a vast number of applications, from membrane separation components to electrodes in electrochemical secondary batteries. However, it also degrades their outstanding mechanical properties.

The determination of the mechanical behavior of single-walled CNTs still is a demanding task. Computational tools, such as Molecular Dynamics (MD), have long been a preferred method for this task [6], due to its cost competitiveness, versatility, and notable accuracy. For example, M. Sammalkorpi and co-workers [7] derived a MD-based analytical expression to relate the Young's modulus with the defect density in CNTs and determined that the tensile strength and critical strain of a CNT decreased by a factor of 2 when a single vacancy is present. B. Bucior et al. [8] constructed models of CNTs with tailored pores and found that the correct pore size can separate gas mixtures with great efficiency. Also using MD, S. Rouhi et al. [9] determined that the Young's modulus of graphenylene nanotubes (porous lattice) is about half of that in similar size CNTs.

One popular family of porous carbon allotropes are graphynes. Graphynes pore's size can vary according to the length of their acetylenic links. For example, the intrinsic pores of graphdiyne can be crossed by H_2 molecules and other small molecules and ions [10]. Recently, tubular graphynes have been synthetized [5]. MD simulations have predicted the mechanical properties of graphynes using increasingly accurate forcefields. M. Li and coworkers [11] used the AIREBO forcefield [12] to calculate the elastic modulus (Y=465 GPa), the fracture strength ($\sigma = 66.77$ GPa) and fracture strain ($e_c = 0.173$) of armchair γ-graphynes at 1 K, while S. Rouhi et al. [13] determined the mechanical properties of armchair and zig-zag γ-graphdiynes of different diameters and lengths, also using AIREBO. They found that (i) armchair γ-graphdiynes have lower elastic modulus (Y∼310 GPa) than zigzag γ-graphdiynes (Y∼260 GPa) and (ii) their elastic modulus drops with the increase of either temperature or aspect ratio (length/diameter). Faria et al. [14] used AIREBO and Reax forcefields (with two different parameterizations) to study the

* Corresponding author.
E-mail addresses: bruno.faria@dep.uminho.pt (B. Faria), nsilvestre@tecnico.ulisboa.pt (N. Silvestre).

https://doi.org/10.1016/j.eml.2022.101893

mechanical properties of armchair and zigzag γ-graphynes and γ-graphdiynes. They conducted a detailed investigation on the influence of angle and bond length on the behavior of strained nanotubes. They pointed out the limitations of each potential in modeling bond alternation in acetylenic links, and concluded that, when this bond alternation is important, the Reax potential with parameterization from Chenoweth et al. [15] is the most appropriate forcefield.

Very recently, in 2019, K. Ikemoto and co-workers [16] synthetized phenine nanotubes (PhNT) for the first time. The building blocks of CNTs are sp^2 carbon atoms. A PhNT can be idealized as a CNT having each sp^2 carbon atom replaced by a 1,3,5-trisubstituted benzene ring (a "phenine" building block). The team of K. Ikemoto and H. Isobe progressed from cyclometa-phenylene (phenine benzene) [17] to phenine corannulene [18] and from there to phenine circulene [19], which finally led to the synthesis of a PhNT segment composed of 40 phenine units [16]. The fusion of such tubular structures can eventually originate nanotubes with different lengths, while doping phenine units, for example with nitrogen (pyridine units), may expand the nanotube's applications range.

The mechanical properties of PhNTs are yet to be explored. Using MD, Yu et al. [20] studied in detail the cross-sectional shape of PhNTs and found that, contrary to CNTs, PhNTs exhibit polygonal cross sections with the number of flat walls dependent on their diameter. They also found that PhNT forests with squared-section have smother buckling than the CNT circular-section forest. They also studied the mechanical properties of PhNTs under uniaxial tension and reached a value Y$\sim$216 GPa which varied slightly with the nanotubes' diameter. The axial strength (σ = 35–40 GPa) and failure strain (e_c = 0.15–0.17) were also calculated. Despite this primary work and innovative results, Yu and co-workers did not specify the nanotube's chirality (from the visualization of Fig. 1(b) in [20], it is supposed to be PhNT with armchair configuration). Moreover, the mechanical properties of PhNTs subjected to (i) compression, (ii) bending and (iii) torsion, is yet to be investigated.

In this work, armchair and zig-zag PhNTs having diameter similar to those synthetized by K. Ikemoto and co-workers [16] but being longer (with six times their length) are modeled by MD, using the Reax forcefield [15] and the AIREBO forcefield [12], to obtain an accurate description of their mechanical behavior. It is known that the Reax forcefield tends to slightly overestimate the elastic modulus and tensile strength in carbon nanostructures, however it can simulate fracture, bond rupture, buckling and other critical instabilities accurately [14,21]. Considering this, Reax is used here to describe bond breaking and structural instabilities mechanisms at 10 K. On the other hand, AIREBO is widely known to model with reasonably accuracy the core mechanical properties of most carbon nanostructures. In this work, AIREBO is employed with the purpose of forcefield performance comparison with Reax at 10 K and then for predicting the mechanical properties of PhNTs at 300 K. In brief, tensile loading is first applied to the PhNTs, and the results are compared with those obtained by Yu et al. [20]. Then, the nanotubes are subjected to compression and their buckling and failure characteristics are unveiled for the first time. Finally, the nanotubes are subjected to bending and torsion loadings and the moment–rotation relations are derived, and the corresponding mechanical properties, such as the bending and torsional stiffness, are computed. Buckling and fracture mechanisms are unveiled for the different loading cases and the different behaviors between armchair and zig-zag nanotubes are highlighted.

2. Computational approach

The PhNTs were modeled according to Fig. 1. The armchair PhNT shown in Fig. 1(a) has 1888 atoms, 96 pores, length L = 100 Å and radius R = 8.2 Å. The zigzag PhNT represented in Fig. 1(b) has 1904 atoms, 98 pores, L = 99 Å and R = 8.35 Å. Fig. 1 also shows zoom-in views of the "phenine" unit's orientation in both armchair and zig-zag PhNTs. Two carbon nanotubes (CNT) geometrically similar to these PhNTs are also modeled for comparison purposes: (i) an armchair (13,13) CNT with 2132 carbon atoms, L = 100 Å and R = 8.8 Å, and a zig-zag (22,0) CNT with 2112 carbon atoms, L = 101 Å and R = 8.7 Å.

All MD simulations were performed in the simulation package LAMMPS (Large-scale Atomic/Molecular Massively Parallel Simulator [22]. The Reax potential, with the parameterization proposed by Chenoweth et al. [15] was used to model carbon–carbon and carbon–hydrogen bonded and non-bonded interactions. Reax is computationally more expensive than AIREBO [12], which is also considered here. In fact, AIREBO has been used with success to model sp^2 carbon bonding in CNTs subjected to different mechanical loadings [23–25]. However, since this paper reports the first study on the mechanical behavior of PhNT's under compression, bending and torsion loadings, the Reax potential was selected to perform simulations at 10 K due to its accuracy to model necking, buckling, kinking, twisting and other failures that can involve bond break. Reax was implemented with a timestep of 0.35 fs for compressive and tensile loadings and 0.25 fs for torsional and bending loadings of both PhNTs and CNTs. These timestep values were within the limits indicated by Jensen et al. [21] to obtain meaningful results in modeling mechanical properties of graphenic structures with Reax. AIREBO was implemented with a timestep of 1 fs at 10 K and 300 K. The temperature is maintained by employing the Nosé–Hoover thermostat [26] with a damping parameter of 100 x timestep in simulations with both forcefields. All simulations were performed within the context of the microcanonical ensemble (NVT).

The loading is applied to "fixed" atoms (atoms not thermostatized) located at the nanotube edges. They are shown in red in Fig. 1: (i) 32 atoms per edge in armchair PhNT; (ii) 91 atoms per edge in zig-zag PhNT; (iii) 52 atoms per edge in armchair CNT; (iv) 66 atoms per edge in zig-zag CNT. Considering the nanotubes are axially aligned with the z direction, both tensile and compressive loads are applied by moving the fixed atoms at both edges in opposite directions at constant strain rate of 6.4 ns^{-1}: both edges move away in the tensile loading and approach each other in the compressive loading (see Fig. 2(a)–(b)). The nanotubes were stretched or shortened by 40 Å at the end of the simulation.

Bending loading was applied by rotating (about the x-axis) the fixed atoms of both edges of the nanotubes. Then, the nanotubes were bent by $\sim$1.5 rad, bringing both ends closer (to avoid axial tension) at a speed of 0.084 rad ps^{-1}. Twisting loading was imposed by rotating (about the z-axis) the fixed atoms of both edges in opposite directions (clockwise and anticlockwise directions in top and bottom edges). The opposite rotations of both edges twisted the nanotubes at a speed of 0.5027 rad ps^{-1}. At the end of the simulation the nanotubes twisted about $\sim$6.5 rad. Both bending and twisting loadings are depicted in Fig. 2(c)–(d).

Non-periodic boundary conditions were considered in the simulations. The conjugate gradient algorithm was used to optimize the initial nanotube configurations, with energy and force tolerances of 10^{-12}. The nanotubes were then equilibrated for 10 ps at 10 K (or accordingly at 300 K).

In the case of tensile and compressive loadings, the virial stress method [27,28] was used to compute the total stress using: $\sigma_{ij} = S_{ij}\Omega^{-1}$, here Ω is the representative volume and S_{ij} is the macroscopic stress tensor. Since the value of nanotube thickness,

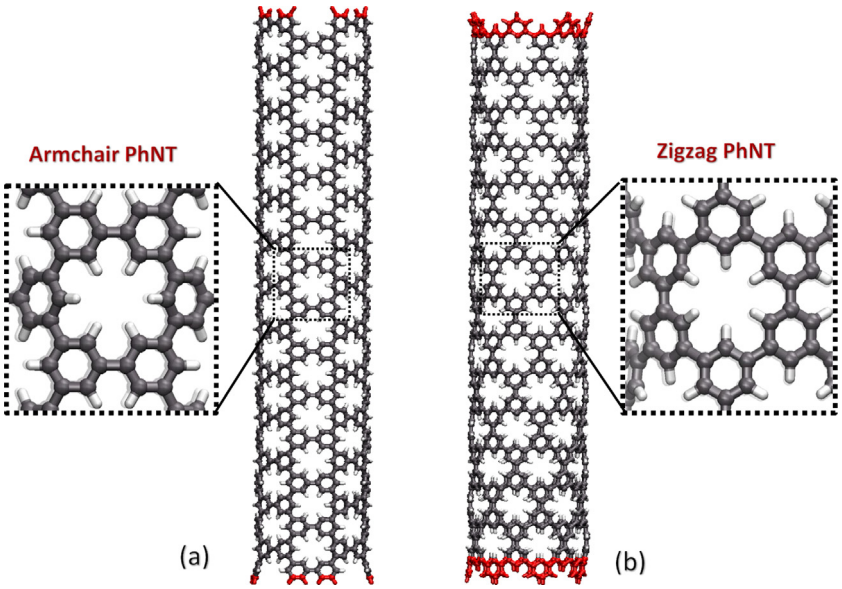

Fig. 1. Atomic models of the (a) armchair (left) and (b) zig-zag (right) PhNTs. Zoom-in views of the pore morphology in both nanotubes.

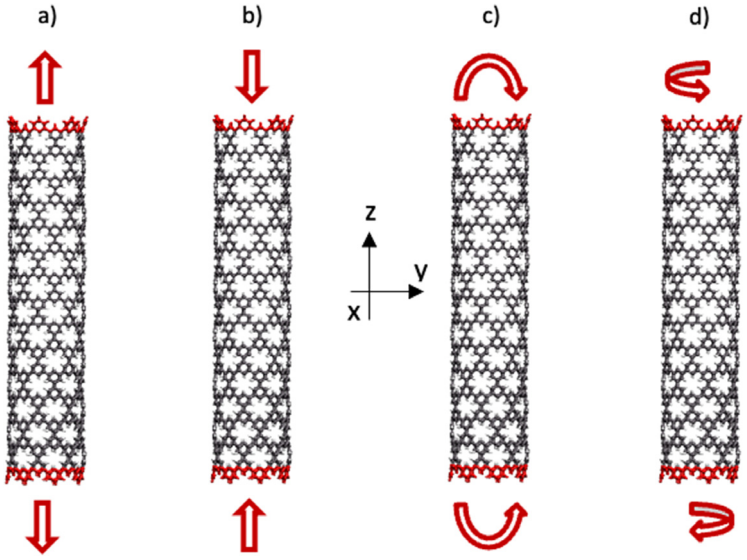

Fig. 2. Loading types: (a) Tension, (b) Compression, (c) Bending, (d) Torsion. "Frozen" atoms in edge boundaries are displayed in red.. (For interpretation of the references to color in this figure legend, the reader is referred to the web version of this article.)

necessary for the calculation of Ω, is not yet an established and consensual issue among the scientific community, some authors [29,30] suggest bypassing the problem by reporting the Young's modulus Y and stress σ in units of force per unit length (N/m). This method for reporting Y and critical strength (σ_c), is adopted here. Note that Y is calculated in the linear (elastic) domain of the stress–strain curve (σ *vs* ε) that corresponds to the quadratic (parabolic) zone of the energy–displacement curve (see Figure S.1, S.2 and S.3 in Supplemental Material, in the average range of $-0.015 < \varepsilon_z < 0.055$). For comparison purposes, the tensile Young's modulus (Y_T) is also calculated using only the data in the positive strain range $0 < \varepsilon_z < 0.055$. In case of bending, the moment M is calculated as the derivative of the potential energy with respect to the bending angle: $M = \partial E/\partial\theta$. In the case of twisting, the torque is calculated as the derivative of the potential energy with respect to the twist: $T = \partial E/\partial\phi$.

3. Results and discussion

3.1. Tensile and compressive behavior of PhNTs

Stress–strain curves obtained for tensile and compressive loading of armchair and zigzag PhNTs at 10 K, using the Reax potential and the AIREBO potential are respectively presented in Fig. 3(a)–(b) and in Fig. 4(a)–(b). Stress–strain curves for identical loading of armchair and zigzag CNTs are also presented in both Figures (dashed lines) enabling a comparison between the mechanical behavior of PhNTs and CNTs from the perspective of both potentials. In addition, the stress–strain curves for CNTs and PhNTs under tensile loading reported in the work of Yu et al. [20] are also depicted in Fig. 3(a), Fig. 4(a) and Fig. 5(a) (red curves) allowing the validation of our implementation of the AIREBO potential. Stress–strain curves obtained for tensile and compressive loading of armchair and zigzag PhNTs at 300 K with AIREBO are presented in

Table 1
Young's modulus (Y in N/m), Tensile Strength (σ_T in N/m), Compressive Strength (σ_C in N/m), failure strain (ε_z) and critical strain (ε_c) of PhNTs at 10K modeled by the Reax potential. The variation percentage of these properties with respect to those of similar CNTs is also shown.

Structure	Y_T	Y	%	Tension			Compression				
				σ_T	%	ε_z	%	σ_C	%	ε_c	%
CNT (armchair)	431	424	–	69.2	–	0.167	–	10.7	–	0.028	–
CNT (zig-zag)	394	417	–	61.7	–	0.165	–	13.2	–	0.034	–
PhNT (armchair)	150	126	−70%	31.0	−55%	0.196	+17%	3.6	−66%	0.036	+29%
PhNT (zig-zag)	110	105	−75%	37.4	−39%	0.212	+28%	2.7	−80%	0.050	+47%

Table 2
Young's modulus (Y in N/m), Tensile Strength (σ_T in N/m), Compressive Strength (σ_C in N/m), failure strain (ε_z) and critical strain (ε_c) of PhNTs at 10K modeled by the AIREBO potential. The variation percentage of these properties with respect to those of similar CNTs is also shown.

Structure	Y_T	Y	%	Tension			Compression				
				σ_T	%	ε_z	%	σ_C	%	ε_c	%
CNT (armchair)	268	264	–	35.4	–	0.172	–	15.5	–	0.047	–
CNT (zig-zag)	302	295	–	30.1	–	0.139	–	19.0	–	0.062	–
PhNT (armchair)	88	84	−68%	9.0	−75%	0.119	−31%	4.4	−71%	0.074	+57%
PhNT (zig-zag)	75	67	−77%	6.2	−79%	0.089	−36%	4.4	−77%	0.106	+72%

Table 3
Young's modulus (Y in N/m), Tensile Strength (σ_T in N/m), Compressive Strength (σ_C in N/m), failure strain (ε_z) and critical strain (ε_c) of PhNTs at 300K modeled by the AIREBO potential. The variation percentage of these properties with respect to those of similar CNTs is also shown.

Structure	Y_T	Y	%	Tension			Compression				
				σ_T	%	ε_z	%	σ_C	%	ε_c	%
CNT (armchair)	249	258	–	35.1	–	0.174	–	13.5	–	0.044	–
CNT (zig-zag)	273	284	–	27.2	–	0.122	–	15.5	–	0.049	–
PhNT (armchair)	83	80	−69%	8.0	−77%	0.107	−39%	4.6	−66%	0.078	+78%
PhNT (zig-zag)	68	61	−78%	4.8	−82%	0.075	−39%	4.4	−72%	0.098	+101%

Fig. 5(a)–(b) showing the mechanical behavior of these nanotubes at room temperature. Table 1 resumes the mechanical properties (Young's modulus, tensile strength, compressive strength, and critical strain) computed for these nanotubes with the Reax forcefield at 10 K. Tables 2 and 3 present the same properties but calculated with the AIREBO potential at 10 K and 300 K, respectively. It should be noted that these Tables show both the Young's modulus calculated exclusively from linear regression in the tensile region (Y_T), and the Young's modulus obtained from linear regression fitted on the elastic compressive and tensile regions (Y) (see Figure S.1–S.3 from Supplemental Information section).

As expected, there are only minor differences between tensile stress–strain curves for both CNTs and PhNTs from the work of Yu et al. [20] and our work since both are modeled by the AIREBO potential. The most notable differences are in the failure strains (see Fig. 4(a)), which are lower in our work (−15% for CNTs and −25% for PhNTs). Beside possible variations in the modeling strategy of both works also the larger diameter of armchair CNTs and PhNTs modeled here may explain the slightly different results ($R_{\mathrm{CNT(Ref20)}}$ and $R_{\mathrm{PhNT(Ref20)}}$ are equal to 8.1 Å).

Regarding tensile and compressive loading, results show that (i) the AIREBO and Reax potentials clearly model nanotubes differently, (ii) both potentials agree that PhNTs are weaker than CNTs (lower Y and tensile strength) but according to Reax PhNTs are more flexible (higher failure strain) than CNTs, (iii) temperature slightly degrades the mechanical properties of both types of nanotubes although this effect is less pronounced in PhNTs.

In tensile loading, Reax predicts increasingly higher stresses for the same strains, when compared to AIREBO for both PhNTs and CNTs (see Fig. 3(a) and 4(a)). For example, Reax predicts a tensile strength of 31.0 N/m and 37.4 N/m for armchair PhNT and zigzag PhNT respectively, while AIREBO predicts a tensile strength of 9.0 N/m and 6.2 N/m for the same nanotubes. In case of CNTs the same trend is present (see Tables 1 and 2). The Young's modulus predicted by Reax for CNTs and PhNTs are also similarly higher than those predicted by AIREBO. However, while Reax predicts similar failure tensile strains for both CNTs ($\varepsilon_z \approx 0.17$), armchair CNTs have higher failure tensile strains than zigzag CNTs according to AIREBO ($\varepsilon_z \approx 0.17$ and $\varepsilon_z \approx 0.14$, respectively). For PhNTs, Reax predicts much higher fracture tensile strains than AIREBO (almost twofold in the case of armchair, and more than twofold in the case of zigzag). From Tables 1–2 and Figs. 3(a)–4(a) it can be found that the Reax potential may overestimate the tensile stress which leads to an overestimation of the mechanical properties of the nanotubes: Reax predicts Y=1285 GPa for armchair CNT and Y=1177 GPa for zig-zag CNT when it is generally accepted that the Y of CNTs is slightly less or equal to 1TPa. On the other hand, it is known that Reax gives a better description of bond rupture in structures with multiple C-hybridizations or with multiple elements bonded to C (in this case we have sp^2 carbons atoms bonded to each other and to hydrogen in a highly porous structure).

Using both potentials, the value of Y for PhNTs is clearly lower than that of their CNTs counterparts: Y of CNTs, using Reax, is close to 420 N/m (difference in Y_T is higher) while that of PhNTs is in average about 110 N/m (drop of about 70%–75%); with AIREBO the Y of CNTs is lower for armchair (Y=264 N/m) than for zig-zag (Y=295 N/m) but also drops by 68%–77% for PhNTs. Irrespectively of forcefield, armchair PhNTs have between 20%–25% higher Y than zig-zag PhNTs.

In fact, PhNTs elastic properties are close to Graphdiyne nanotubes (GDYNTs). Using an identical tensile loading method and forcefield (Reax with parameterization by Chenoweth *et* [15]), but for slightly longer nanotubes, the authors [14] found Y= 156 N/m for armchair GDYNTs and Y=141.5 N/m for zig-zag GDYNTs. In the case of armchair nanotubes, these values are close to the Y_T calculated and shown in Table 1.

The tensile strength (σ_T) of PhNTs was also found to be much lower than the σ_T of CNTs (drop between 39% and 55% with Reax and between 75 and 77% with AIREBO). However, with Reax, contrary to CNTs, zig-zag PhNTs have a higher σ_T than armchair ones (increase of 20%). The failure strain, with this potential, is also notably higher for PhNTs than for CNTs (rise between 17%

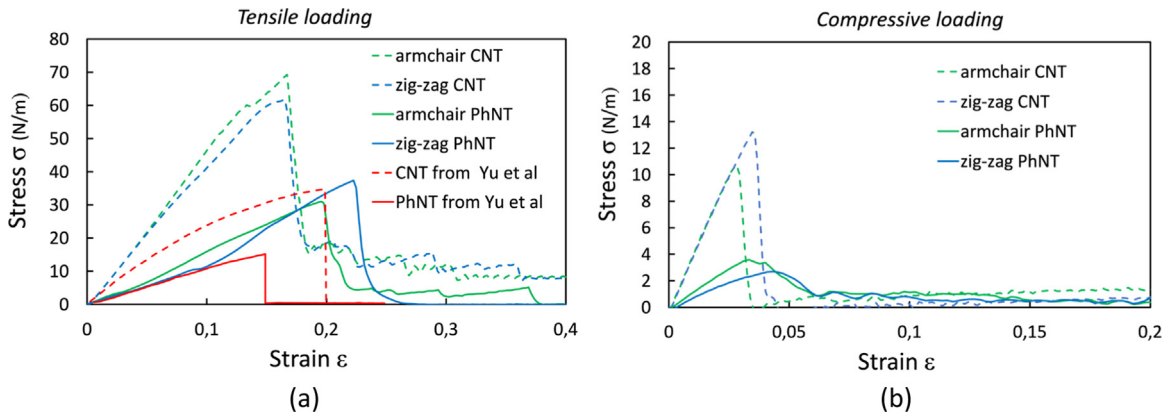

Fig. 3. Stress–strain variation for armchair (green curve) and zig-zag (blue curve) PhNTs and comparison with armchair (green dashed curve) and zig-zag (blue dashed curve) CNT of similar dimensions for (a) tensile and (b) compressive loadings using the Reax potential at 10 K. Tensile stress–strain variation for CNTs and PhNTs with diameters of 16.2 Å from the work of *Yu et al.* [20] are also shown in Fig. 3(a).. (For interpretation of the references to color in this figure legend, the reader is referred to the web version of this article.)

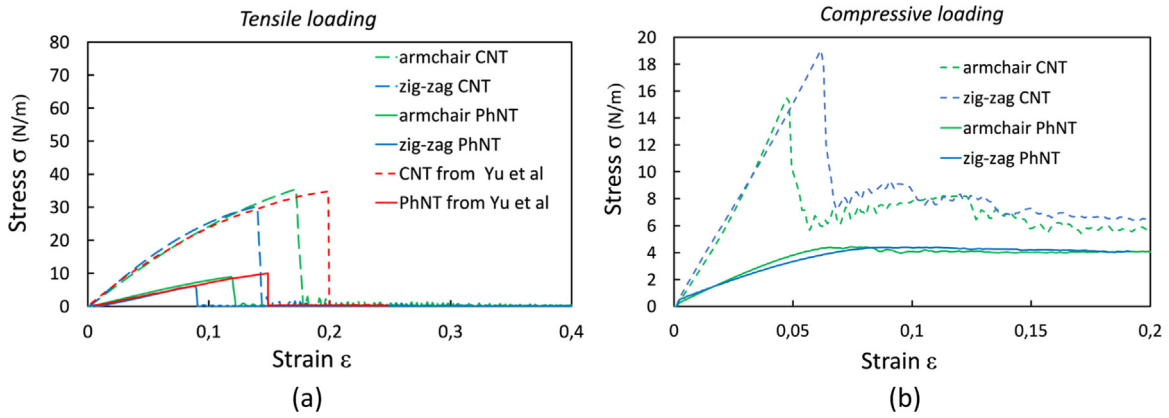

Fig. 4. Stress–strain variation for armchair (green curve) and zig-zag (blue curve) PhNTs and comparison with armchair (green dashed curve) and zig-zag (blue dashed curve) CNT of similar dimensions for (a) tensile and (b) compressive loadings using the AIREBO potential at 10 K. Tensile stress–strain variation for CNTs and PhNTs with diameters of 16.2 Å from the work of *Yu et al.* [20] are also shown in Fig. 4(a).. (For interpretation of the references to color in this figure legend, the reader is referred to the web version of this article.)

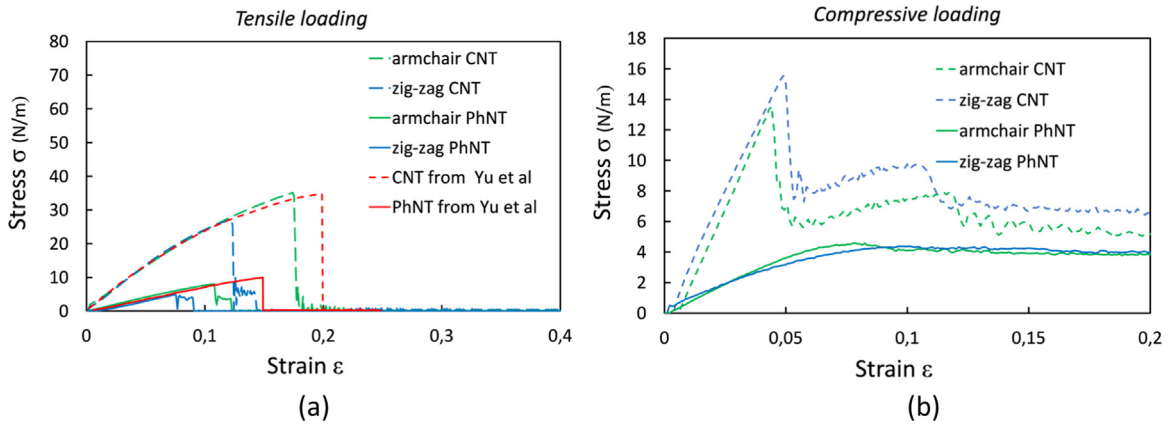

Fig. 5. Stress–strain variation for armchair (green curve) and zig-zag (blue curve) PhNTs and comparison with armchair (green dashed curve) and zig-zag (blue dashed curve) CNT of similar dimensions for (a) tensile and (b) compressive loadings using the AIREBO potential at 300 K. Tensile stress–strain variation for CNTs and PhNTs with diameters of 16.2 Å from the work of *Yu et al.* [20] are also shown in Fig. 5(a).. (For interpretation of the references to color in this figure legend, the reader is referred to the web version of this article.)

and 28%), which means that they can endure longer stretching without failure. Contrary to Reax, AIREBO predicts lower tensile strains for PhNTs than for CNTs (between 31%–36% lower, see Tables 1 and 2).

In compression, Reax systematically predicts lower stress for identical strains when compared to AIREBO. With Reax, armchair PhNTs present a higher compressive strength than zigzag PhNTs (33% higher) while for AIREBO armchair PhNTs present an

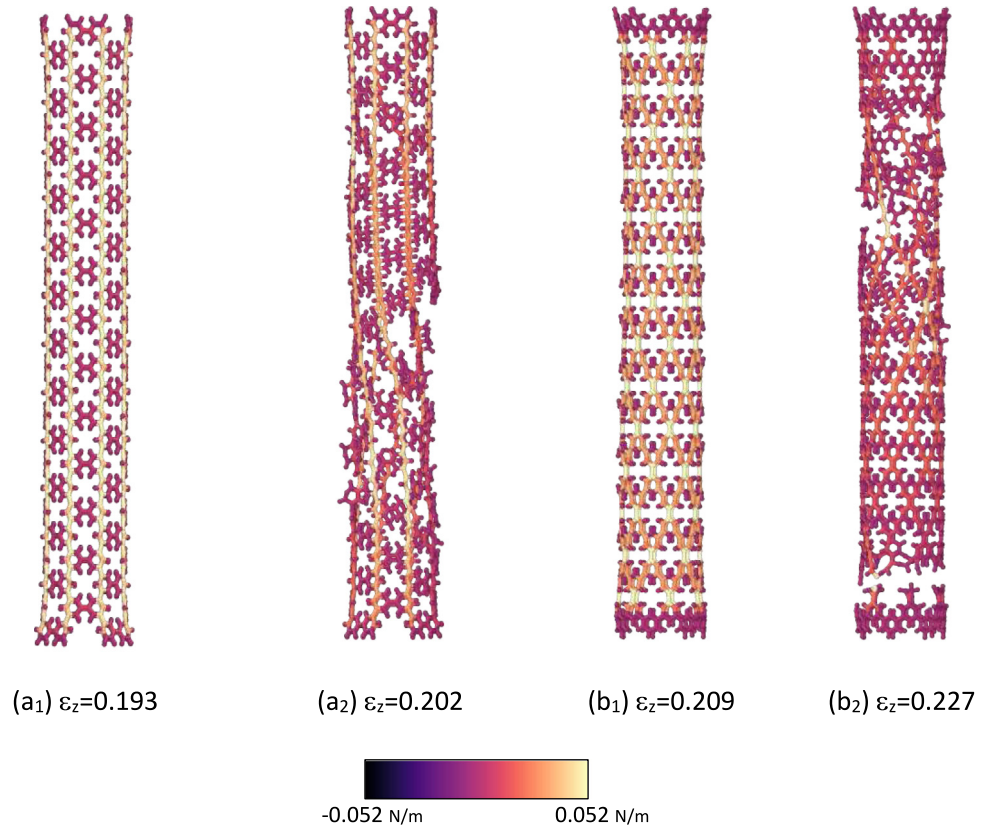

Fig. 6. Stress distribution in tensile loading of (a) armchair PhNT and (b) zigzag PhNT, immediately before (1) and after (2) rupture.

identical compressive strength than zig-zag, but between 22%–62% higher than that calculated by Reax. It is noted that both PhNTs are much weaker in compression than the CNTs (between 66% and 80% weaker for both potentials). Similarly to tension with Reax (but contrary to tension with AIREBO), PhNTs under compression can endure longer strains without buckling, since their critical strains are higher than CNTs (between 29% and 47% with Reax, and between 57%–72% with AIREBO).

Table 3 shows the mechanical properties of PhNTs calculated for tensile loading and compressive loading with the AIREBO potential at 300 K, while the respective stress–strain curves are represented in Fig. 5(a)–(b). It is notable that the effect of increasing the temperature is a slight deterioration of the Y (−2.2% in armchair CNT, −3.7% in zigzag CNT, −4.8% in armchair PhNT and 9.0% in zig-zag PhNT); of the tensile strength (average decline between 1%–23%; of the compressive strength (average decline between 0–18.5%); of the failure strains (average decline between 1–18.6%) and of critical strains (average decline between 6.8%–26%).

Bond rupture mechanisms obtained using the Reax potential at 10 K are shown next. Fig. 6 shows the stress distribution in armchair PhNT (Fig. 6(a)) and zigzag PhNT (Fig. 6(b)) before tensile failure (case 1) and immediately after tensile failure (case 2). In tensile loading, the armchair lattice configuration is spatially rearranged in such a manner that there is a set of bonds closely aligned with the direction of the imposed load. These bonds connect the phenine units and can be seen as forming longitudinal stress lines (yellow chains) along the length of the nanotube. Naturally, these yellow bond chains act like a set of longitudinal strings that carry most of the tensile load, as can be seen in Fig. 6(a1). The bonds in red are transversally compressed due to Poisson's effect. The rupture of the bonds of these longitudinal chains leads to fracture of the PhNT, as seen in Fig. 6(a2).

The detailed first bond rupture mechanism is shown is Fig. 7. One of the bonds in the longitudinal chains, where local stress is higher, breaks, leading to an immediate stress drop in neighbor carbon atoms. This precipitates more bond breaking in adjacent longitudinal stress chains. Fig. 7(a1) (a2) and (a3) depict stresses and strains involved in this bond breaking.

In case of zigzag PhNTs, the tensile loading is more distributed as it is observed in Fig. 6(b_1). The tensile loading results now in a network of yellow and orange bond chains that are tensioned. This diamond-shaped network of tensioned bonds turns the zigzag PhNTs more flexible than the armchair PhNT (lower Y) but also turns it more resistant than armchair PhNT because it has higher tensile strength σ_T and slightly higher failure strain ε_z. From the stress–strain curves of Fig. 3(a), it can be observed that the "activation" of these tensile bond chains explains the sudden hardening of the zig-zag PhNT (blue curve) for strains above 0.1 ($\varepsilon_z > 0.1$).

The rupture mechanism for zigzag PhNT under tensile loading, which differs from the case of armchair tensile loading, is represented in Fig. 8. Bond rupture occurs when a new bond is formed between the two non-adjacent carbon atoms that are close neighbors to the carbon atom that connects two longitudinally adjacent phenine units (represented in yellow, heavily stressed, in Fig. 8(a_1) and (a_2)). Since these two non-adjacent carbon atoms are brought closer due to the deformation of the phenine unit, they establish a bond which (due to the sp^2 preferable conformation) induces the two adjacent bonds in the interior of the phenine unit to break. This mechanism is shown in detail in the sequence (a_1)–(a_2)–(a_3) of Fig. 8, where the stresses and strains at the onset of bond breaking are also depicted.

Fig. 9 shows the stress distribution in armchair PhNT (Fig. 9(a)) and zigzag PhNT (Fig. 9(b)) before compressive buckling (case 1) and immediately after compressive buckling (case 2) calculated by the Reax forcefield. The most stressed bonds in compressive

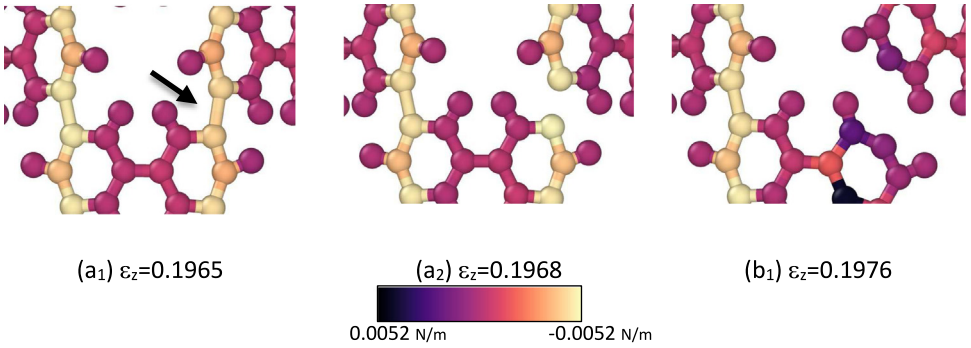

Fig. 7. First bond rupture mechanism in tensile loading of armchair PhNT with representation of local stress. The black arrow point to the C–C bond that connects two phenine units and that is about to break. The sequence (a1)(a2)(a3) shows the bond rupture mechanism and respective stress and strains associated.

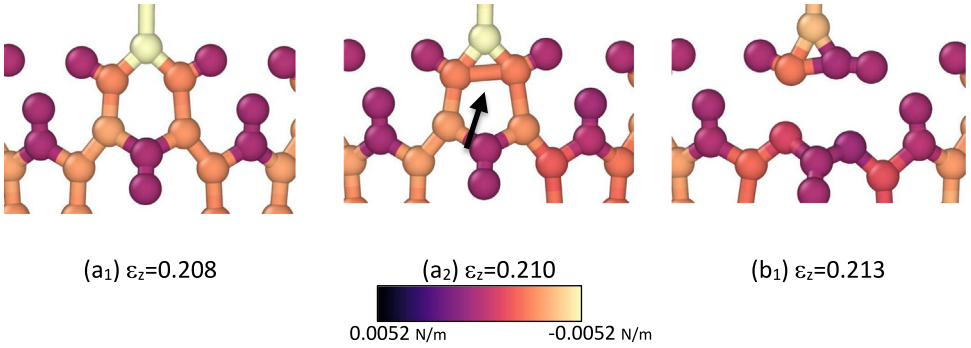

Fig. 8. First bond rupture mechanism in tensile loading of zigzag PhNT with representation of local stress. The black arrow points to the C–C bond that emerges connecting two non-adjacent carbon atoms inside the phenine unit leading to the break of two neighbor C–C bonds inside that phenine unit. The sequence (a1)(a2)(a3) shows the bond rupture mechanism and respective stress and strains associated.

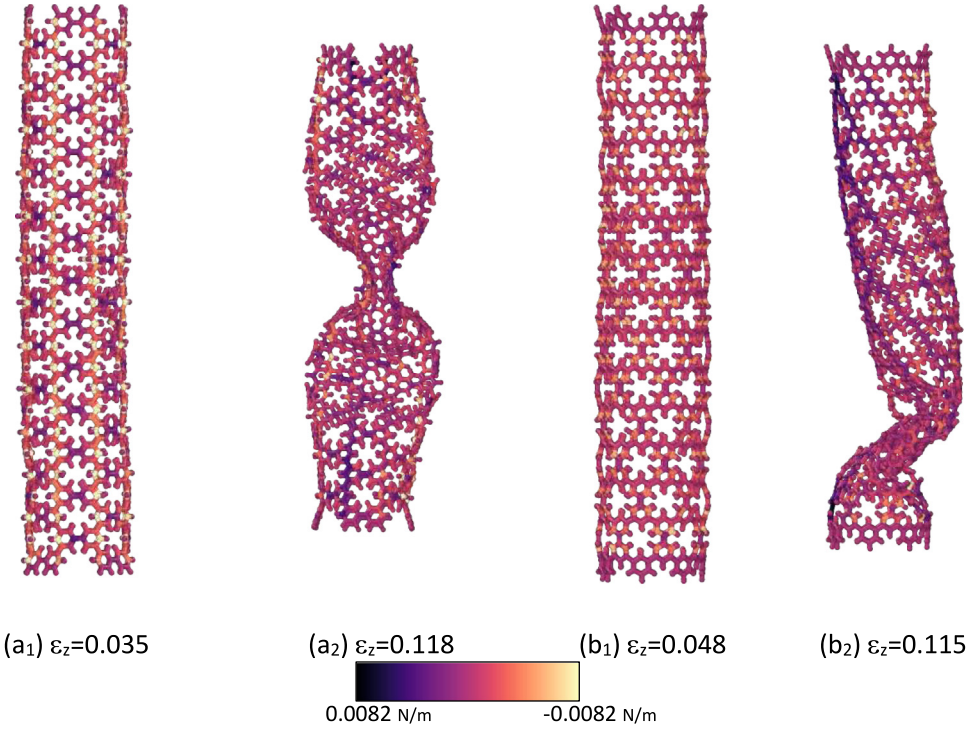

Fig. 9. Stress (σ_z) distribution in compressive loading of a) armchair PhNT and b) zigzag PhNT, before critical strain (1) and after buckling (2).

loading coincide with those that are also the most stressed in tensile loading, particularly those belonging to aromatic rings.

Analogously to tensile loading, the bonds directly aligned with the direction of compression are the most compressed ones. Compressive load distribution remains more efficient in zigzag PhNTs since more bonds are strained along the diamond-shape network. This is translated into a higher critical strain for zigzag PhNTs ($\varepsilon_c = 0.050$) than for armchair PhNTs ($\varepsilon_c = 0.036$).

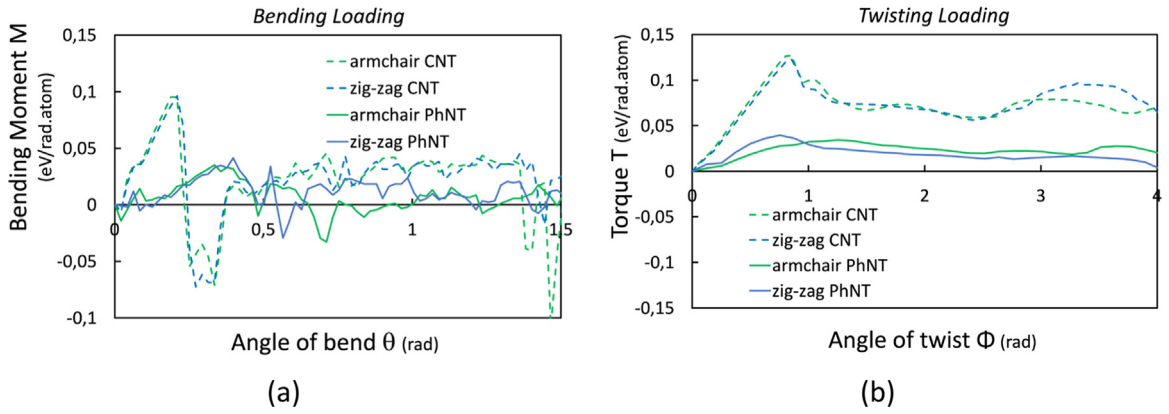

Fig. 10. Variation of Bending Moment/Torque with the Angle of Bend/Twist for armchair PhNT (green curve) and zig-zag PhNT (blue curve) and comparison with armchair CNT (green dashed curve) and zig-zag CNT (blue dashed curve) of similar dimensions at 10 K and using the Reax forcefield for (a) bending deformations and (b) twisting deformations.. (For interpretation of the references to color in this figure legend, the reader is referred to the web version of this article.)

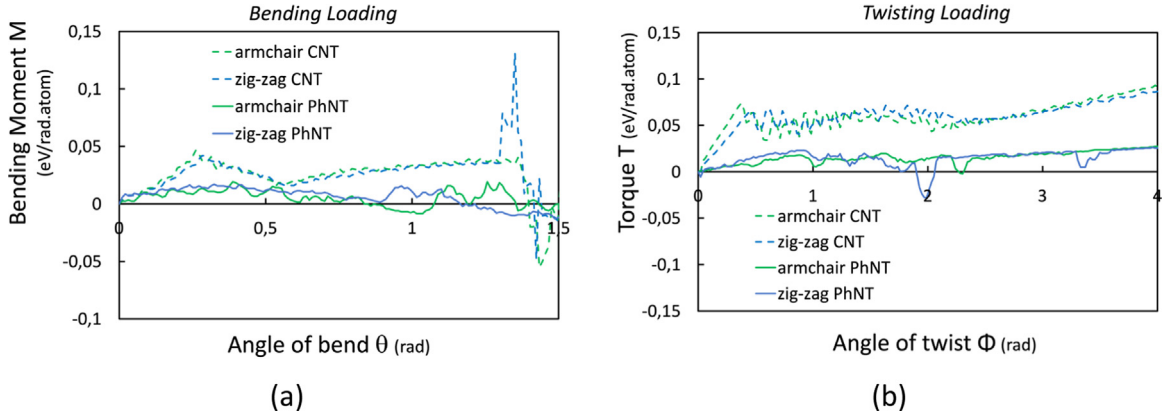

Fig. 11. Variation of Bending Moment/Torque with the Angle of Bend/Twist for armchair PhNT (green curve) and zig-zag PhNT (blue curve) and comparison with armchair CNT (green dashed curve) and zig-zag CNT (blue dashed curve) of similar dimensions at 10 K and using the AIREBO potential for (a) bending deformations and (b) twisting deformations.. (For interpretation of the references to color in this figure legend, the reader is referred to the web version of this article.)

However, zigzag PhNTs have lower critical stress ($\sigma_C = 2.7$ N/m) than armchair PhNTs ($\sigma_C = 3.6$ N/m) because the side walls of the zigzag PhNT show very small waves (see Fig. 9(b1)) that trigger a smooth buckling — note also that the Young's modulus of zigzag PhNT is also proportionally lower than that of armchair PhNT (105 N/m vs. 126 N/m).

3.2. Bending and twisting of phenine nanotubes

In this section, the bending and twisting behaviors of armchair and zigzag PhNTs modeled with the Reax and the AIREBO potential are presented. The bending moment was obtained from the first derivative of potential energy w.r.t the angle of bend and is represented in Fig. 10(a) for armchair and zig-zag PhNTs as well as for CNTs of identical chirality modeled by the Reax potential at 10 K. In Figs. 11(a) and 12(a), similar results are presented for the same nanotubes but modeled with the AIREBO potential at 10 K and 300 K, respectively.

In case of both PhNTs and CNTs at 10 K under bending, the Reax potential predicts a higher bending stiffness and a higher bending moment than the AIREBO potential. On the other hand, Reax predicts a slightly lower critical angle of bend (except for zigzag PhNT) when compared to AIREBO. The exact differences between the two potentials can be clearly seen in Tables 4 and 5. PhNTs show a lower bending stiffness (around 80% less, independently of the potential employed) when compared to CNTs, so they are much easier to bend than CNTs, due their porosity. The slopes of the ascending path of curves in Fig. 10(a) and Fig. 11(a) show this evidence.

However, PhNTs tolerate higher angles of bend without bond rupture than CNTs: armchair CNTs buckle abruptly at $\theta_c = 0.19$ rad (Reax) or $\theta_c = 0.26$ rad (AIREBO) and zigzag CNTs buckle at $\theta_c = 0.21$ rad (Reax) or $\theta_c = 0.28$ rad (AIREBO) while PhNTs only buckle at $\theta_c = 0.33$ rad (armchair) and at $\theta_c = 0.36$ rad (zigzag) with Reax and at $\theta_c = 0.39$ rad (armchair) and at $\theta_c = 0.23$ rad (zigzag) with AIREBO, as can be seen from Tables 4 and 5.

The Young's modulus can be computed from the elasticity formula $Y = M/(I\chi)$, where χ is the angle of bend per unit of length of the nanotube ($\chi = \theta/L$, usually designated as curvature) and I is the second moment of area of the nanotube cross-section ($I = \pi R^3 t + \frac{1}{4}\pi R t^3$), where R and t are the nanotube's radius and thickness (for consistency with the literature, we have adopted $t = 0.34$ nm [24]. The Young's modulus Y_b was computed from the initial ascending path (elastic) of each $M(\theta)$ curve. These data are shown in Tables 4 and 5, as well as the bending stiffness $K = \partial M/\partial\chi = YI$.

The values of Young's modulus Y_b obtained from the bending tests are lower than those calculated from tensile and compressive loading tests (Y), being more sensitive to the nanotubes' chirality, with exception for Y_b for zig-zag PhNT for AIREBO which is 31% higher than Y.

Fig. 13 shows a visual representation of the bending deformation of PhNTs at two different angles of bend calculated from Reax. It can be observed that the armchair PhNT shows a greater number of kinks than zigzag PhNT for an angle of bend around

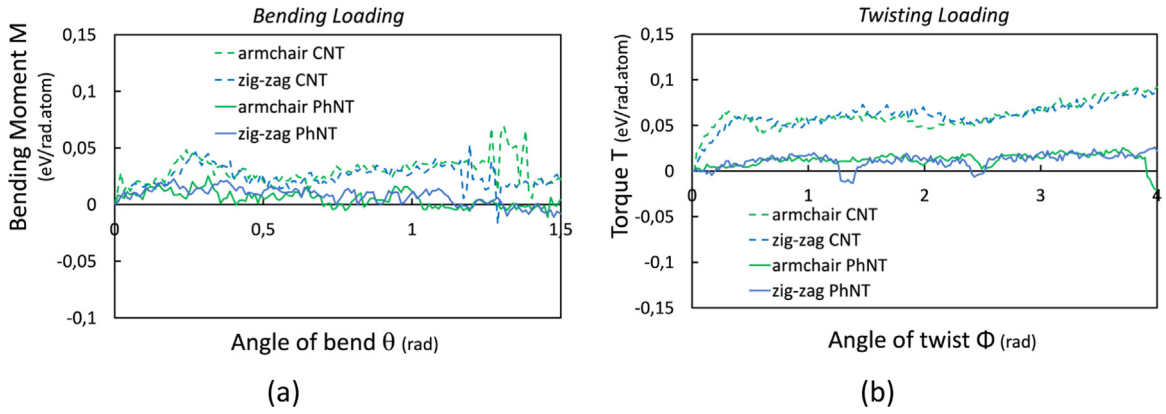

Fig. 12. Variation of Bending Moment/Torque with the Angle of Bend/Twist for armchair PhNT (green curve) and zig-zag PhNT (blue curve) and comparison with armchair CNT (green dashed curve) and zig-zag CNT (blue dashed curve) of similar dimensions at 300 K and using the AIREBO forcefield for (a) bending deformations and (b) twisting deformations.. (For interpretation of the references to color in this figure legend, the reader is referred to the web version of this article.)

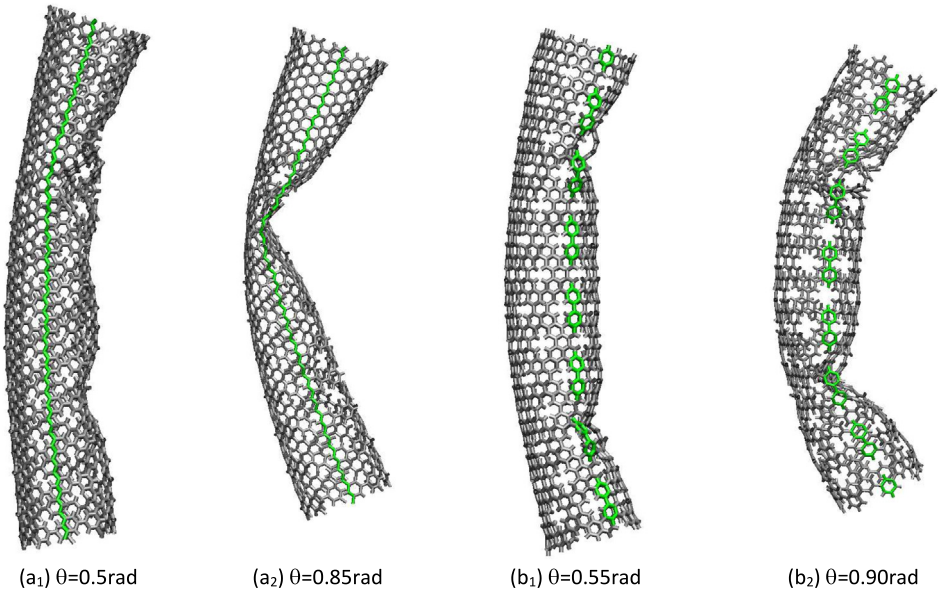

Fig. 13. Visual representation of bending loading of a) armchair PhNT and b) zig-zag PhNT, near the critical angle of bend (1) and after the critical angle of bend (2) with Reax at 10 K. Bonds aligned with a straight longitudinal line are colored green, so that after bending, the colored bonds can give a 3D perception of the deformation of PhNTs resulting from bending.. (For interpretation of the references to color in this figure legend, the reader is referred to the web version of this article.)

Table 4
Bending Stiffness (K) in eV um, bending Young's modulus (Y_b) in GPa, tensile compressive Young's modulus (Y) in GPa (obtained from Table 1 but considering a nanotube thickness of 0.34 nm), maximum Bending Moment ($M_{máx}$) in eV rad^{-1} and critical angle of bend (θ_c) in rad, of PhNTs and similar length and diameter carbon nanotubes for bending mechanical tests using the Reax potential at 10 K. The Young's modulus obtained from bending are compared with that obtained from tensile-compressive tests, while $M_{máx}$ and θ_c are compared between CNTs and PhNTs.

Structure	K	Y_b	Y	% (Y_b/Y)	M_{max}	%	θ_c	%
CNT (armchair)	5.234	1058	1285	−18	203.07	–	0.19	–
CNT (zig-zag)	4.820	1024	1177	−13	184.42	–	0.21	–
PhNT (armchair)	1.072	286	448	−36	66.31		0.33	+78
PhNT (zig-zag)	1.249	305	327	−7	62.2		0.36	+70

Table 5
Bending Stiffness (K) in eV um, bending Young's modulus (Y_b) in GPa, tensile compressive Young's modulus (Y) in GPa (obtained from Table 2 but considering a nanotube thickness of 0.34 nm), maximum Bending Moment ($M_{máx}$) in eV rad^{-1} and critical angle of bend (θ_c) in rad, of PhNTs and similar length and diameter carbon nanotubes for bending mechanical tests using the AIREBO potential at 10K. The Young's modulus obtained from bending are compared with that obtained from tensile-compressive tests, while $M_{máx}$ and θ_c are compared between CNTs and PhNTs.

Structure	K	Y_b	Y	% (Y_b/Y)	M_{max}	%	θ_c	%
CNT (armchair)	3.068	620	800	−23	99.59	–	0.26	–
CNT (zig-zag)	2.500	531	901	−41	88.67	–	0.28	–
PhNT (armchair)	0.540	144	262	−45	36.61	−63	0.39	+48
PhNT (zig-zag)	0.404	99	75	+31	32.74	−63	0.23	+15

Table 6
Bending Stiffness (K) in eV um, bending Young's modulus (Y_b) in GPa, tensile compressive Young's modulus (Y) in GPa (obtained from Table 3 but considering a nanotube thickness of 0.34 nm), maximum Bending Moment ($M_{máx}$) in eV rad^{-1} and critical angle of bend (θ_c) in rad, of PhNTs and similar length and diameter carbon nanotubes for bending mechanical tests using the AIREBO potential at 300 K. The Young's modulus obtained from bending are compared with that obtained from tensile-compressive tests, while M_{max} and θ_c are compared between CNTs and PhNTs.

Structure	K	Y_b	Y	% (Y_b/Y)	M_{max}	%	θ_c	%
CNT (armchair)	2.624	530	744	−29	102.92	–	0.24	–
CNT (zig-zag)	2.617	556	815	−32	97.62	–	0.27	–
PhNT (armchair)	0.542	145	249	−42	38.20	−63	0.26	+9
PhNT (zig-zag)	0.514	125	68	+85	42.97	−56	0.20	−27

0.5 rad. The latter tends to preserve the cylindrical shape of the nanotube, with the kinks formed close to the ends (edges) of the PhNT.

Similarly to the tensile and compressive behavior, also the bending behavior of nanotubes at 300 K (calculated with AIREBO) degrades when compared to the bending behavior at 10 K. This can be concluded form the observation of Table 6 and comparing it to Tables 4 and 5. The bending stiffness of armchair CNT and zigzag PhNT are lower at 300, but K of zigzag CNT and armchair PhNT have very small increases. In general, the maximum bending moment also decreases for all nanotubes, with exception to armchair CNT which shows a very mild increase. The critical angle of bend is lower at 300 K for the considered nanotubes, most evidently for the phenine nanotubes.

In the case of twisting, the torque T is calculated as the first derivative of potential energy w.r.t the angle of twist ϕ. The variation $T(\phi)$ is represented in Fig. 10(b) (Reax) and in Fig. 11(b) (AIREBO) for armchair and zig-zag PhNTs and also for armchair and zig-zag CNTs (dashed lines). It is easily seen in Fig. 10(b), and also in Fig. 11(b) that the slopes of ascending paths of $T(\phi)$ curves are much more pronounced for CNTs than for PhNTs, which is expected due to the high porosity of the latter. Likewise, the maximum torsional strength (see Tables 7 and 8) is also much higher for CNTs than PhNTs. The difference in these properties between CNTs and PhNTs are more notable from the results of AIREBO.

With Reax torque is somewhat higher than with AIREBO. CNTs exhibit a huge drop in torque after the peak (corresponding to the ovalization of the nanotubes' sidewalls and consequent loss of torsional stiffness) but can maintain a more or less constant torque during twist (they do not tear apart for $\phi < 6$ rad). PhNTs do not show such brittle behavior: their torsional stiffness is much lower and torque slowly decreases with increasing twist, meaning that although ovalized they retain some torsional stiffness (see Fig. 10(b). With AIREBO the twisting behavior of CNTs has a clearer trend (similar in both configurations): torque increases until maximum torque ($T_{\max} = 0.074$ eV/rad atom) and then slightly drops (0.39 rad $< \phi <$ 0.9 rad) and then tends to steadily increase until ultimately drop at $\phi = 4.56$. The trend can be explained by the sudden decrease in torsional stiffness when the nanotubes' sidewalls ovalize. Contrary to Reax, AIREBO predict that this ovalization slightly increases torque, which means that further twisting increases the tubes' now very low torsional stiffness. With Reax zigzag PhNT has a critical angle of twist ($\phi_c = 0.754$ rad) slightly lower than the CNTs ($\phi_c = 0.854$ rad), but the armchair PhNT has the highest critical angle of twist ($\phi_c = 1.250$ rad). AIREBO predicts lower critical angles of twist for the CNTs and armchair PhNT but a slightly higher critical angle of twist for zigzag PhNT (see Table 8).

For the calculation of mechanical properties, the shear modulus is computed from the elasticity formula $G = T/(J\alpha)$, where α is the angle of twist per unit of length of the nanotube ($\alpha = \phi/L$) and J is the torsional constant ($J = 2\pi R^3 t + \frac{\pi}{2} R t^3$), where R and t are the nanotube's radius and thickness. For consistency with the literature, we have adopted $t = 0,34$ nm [24]. The shear modulus G was computed from the initial ascending path (elastic) of each ($T\phi$) curve. These data are shown in Table 7 (Reax) and Table 8 (AIREBO), as well as the torsional stiffness $K_T = \partial T/\partial\alpha = GJ$.

When modeled with Reax, the torsional stiffness K_T of PhNTs is lower that of CNTs (drops of 83% and 68% for armchair and zigzag), which means that PhNTs porosity allows an increased flexibility to torsion loading. In fact, the shear modulus of armchair CNTs is 4.5 times that of armchair PhNTs, while the shear modulus of zigzag CNTs is 2.6 times that of zigzag PhNTs. With AIREBO the torsional stiffness of PhNTs is also much lower than that of CNTs (drops of 91% and 85% for armchair and zigzag). The shear modulus of armchair CNTs is more than 8 times that of armchair PhNTs, while the shear modulus of zigzag CNTs is more than 5 times that of zigzag PhNTs.

Armchair PhNTs exhibit several differences in their mechanical properties when compared to zigzag PhNTs. Reax predicts that zigzag PhNTs are stiffer and slightly harder to twist than armchair PhNTs, but that these fail for higher angles of twist (almost double), see Table 7. AIREBO predicts zigzag PhNTs to be only slightly stiffer than armchair PhNTs but that both fail for similar angles of twist, see Table 8.

The effect of temperature in twisting can be observed in Table 9, where the mechanical twist properties of the nanotubes calculated from AIREBO at 300 K are shown. With exception for armchair CNT, generally G, K_T, $T_{\max}$, and the critical angle of twist degrade with temperature. However, armchair CNT shows a 10% improvement in G and K_T, while zigzag PhNT shows a 21% increase in the critical angle of twist.

In Fig. 14 it can be clearly seen that the armchair lattice endures much more twisting without rupture than the zigzag one. In Fig. 6 it was observed that tensile loading was mainly stressing longitudinal chains of atoms that connected the structure along the length of the tube. While in tensile loading, these chains were detrimental to achieving higher failure tensile strains, in twisting they are responsible for allowing higher critical angles of twist, since they permit more twisting without bond breaking.

3.3. Assessment of elastic buckling formulas

Since the earlier works on the buckling behavior of CNTs, many works have been published about the application of shell buckling formulas to the prediction of critical loads and moments [31] To a minor extent, the authors have contributed to the current state-of-the-art [32–34] In this work, we apply the elastic buckling formulas based on thin-shell theories (Donnell–Sanders) to estimate the (i) critical stress σ_c (compression), (ii) critical moment M_c (bending) and (iii) critical torque T_c (twisting), and evaluate their accuracy. According to Silvestre [32–34] the following formulas are given

$$\sigma_c = \frac{Y}{\sqrt{3\left(1-\nu^2\right)}}\frac{t}{R} \tag{1}$$

$$M_c = K\frac{\sqrt{1-\nu^2}}{\sqrt{3}}\frac{t}{R^2} \tag{2}$$

$$T_c = K_T\frac{0.236Y}{GR\left(1-\nu^2\right)^{0.75}}\left(\frac{t}{R}\right)^{1.5} \tag{3}$$

Table 7
Shear Modulus (G) in TPa, Torsion constant (J) in nm^4, Torsional Stiffness (K_T) in eV um, maximum Torque (T_{max}) in eV/rad and critical angle of twist (ϕ_c) in rad, of PhNTs with comparison (in percentage) to similar length and diameter CNTs for twisting mechanical tests modeled with the Reax potential at 10 K.

Structure	G	J	K_T	%	T_{max}	%	ϕ_c	%
CNT (armchair)	0.308	1.64	2.933	–	271.1	–	0.854	–
CNT (zig-zag)	0.312	1.56	2.852	–	259.0	–	0.854	–
PhNT (armchair)	0.069	1.25	0.506	−83	64.9	−73	1.250	+46
PhNT (zig-zag)	0.116	1.36	0.911	−68	75.3	−68	0.754	−12

Table 8
Shear Modulus (G) in TPa, Torsion constant (J) in nm^4, Torsional Stiffness (K_T) in eV um, maximum Torque (T_{max}) in eV/rad and critical angle of twist (ϕ_c) in rad, of PhNTs with comparison (in percentage) to similar length and diameter CNTs for twisting mechanical tests modeled with the AIREBO potential at 10 K.

Structure	G	J	K_T	%	T_{max}	%	ϕ_c	%
CNT (armchair)	0.363	1.64	3.451	–	157.6	–	0.377	–
CNT (zig-zag)	0.293	1.56	2.677	–	140.1	–	0.461	–
PhNT (armchair)	0.042	1.25	0.305	−91	34.4	−75	0.880	+133
PhNT (zig-zag)	0.051	1.36	0.406	−85	44.2	−65	0.859	+86

Table 9
Shear Modulus (G) in TPa, Torsion constant (J) in nm^4, Torsional Stiffness (K_T) in eV um, maximum Torque (T_{max}) in eV/rad and critical angle of twist (ϕ_c) in rad, of PhNTs with comparison (in percentage) to similar length and diameter CNTs for twisting mechanical tests modeled with the AIREBO potential at 300K.

Structure	G	J	K_T	%	T_{max}	%	ϕ_c	%
CNT (armchair)	0.400	1.64	3.807	–	140.5	–	0.272	–
CNT (zig-zag)	0.242	1.56	2.090	–	125.7	–	0.398	–
PhNT (armchair)	0.036	1.25	0.268	−93	26.5	−79	0.712	+162
PhNT (zig-zag)	0.041	1.36	0.324	−85	38.2	−66	1.047	+163

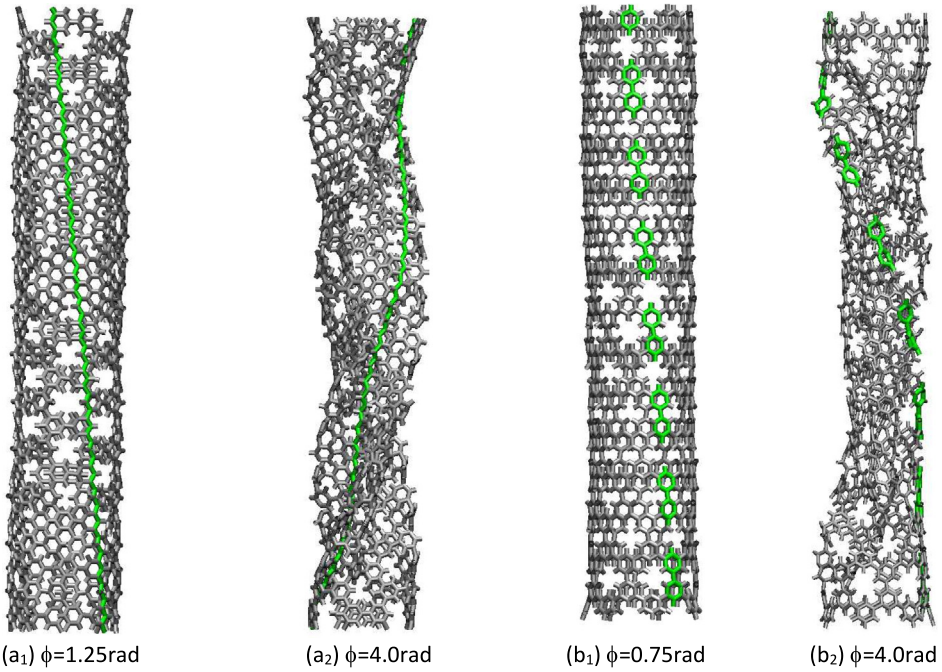

Fig. 14. Visual representation of twisting loading of (a) armchair PhNT and (b) zig-zag PhNT, at critical angle of twist (maximum torque) (1) and after the critical angle of twist (2) (with Reax at 10 K). Bonds aligned with a straight longitudinal line are colored green, so that after the imposition of twisting loading, the colored bonds can give a 3D perception of the twisted deformation of PhNTs.. (For interpretation of the references to color in this figure legend, the reader is referred to the web version of this article.)

where the several variables were provided before in Tables 1 to 9. The generally accepted Poisson ratio $\nu = 0.20$ of graphene and carbon X-enes was adopted, as well as the equivalent shell thickness $t = 0.66$ Å proposed by Yakobson et al. [35] and widely applied [31]. The application of these simple elastic buckling formulae to the CNTs and PhNTs studied in this work, leads to the values of critical stress σ_c (compression), critical moment M_c (bending) and critical torque T_c (twisting), shown in Table 10, for the Force Fields (FF) and temperatures (T) considered.

Overall, the elastic buckling formulas provide a fair qualitative measure and trend of the critical variables. In case of compression, the MD-to-analytical critical stress ratio varies between 55% and 155%, the worst and best cases being those of Reax-10K (40% difference in average) and AIREBO-300K (20% difference in average), respectively. In compression, there is no noticeable difference between the errors associated to CNTs and PhNTs, but we may conclude that the analytical predictions are much higher than those given by MD when Reax-10K is adopted. Conversely,

Table 10
Values of critical stress σ_c (in N/m), critical moment M_c (in eV) and critical torque T_c (in eV), obtained from elastic buckling formulas and MD, for different Force Fields (FF) and temperatures (T).

Force field temperature	Structure	σ_C		M_C		T_C	
		MD	(1)	MD	(2)	MD	(3)
Reax 10 K	CNT (armchair)	10.7	18.7	203	252	271	347
	CNT (zig-zag)	13.2	18.6	184	238	259	337
	PhNT (armchair)	3.6	6.0	66.3	59.5	64.9	94.9
	PhNT (zig-zag)	2.7	4.9	62.2	66.9	75.3	80.9
AIREBO 10 K	CNT (armchair)	15.5	11.7	99.6	147.9	157.6	216
	CNT (zig-zag)	19.0	13.2	88.7	123.3	140.1	238
	PhNT (armchair)	4.4	4.0	36.6	30.0	34.4	62.6
	PhNT (zig-zag)	4.4	3.1	32.7	21.6	44.2	52.3
AIREBO 300 K	CNT (armchair)	13.5	11.4	102.9	126.5	140.5	211
	CNT (zig-zag)	15.5	12.7	97.6	129.1	125.7	217
	PhNT (armchair)	4.6	3.8	38.2	30.1	26.5	61.1
	PhNT (zig-zag)	4.4	2.8	43.0	27.5	38.2	47.3

the analytical predictions are always lower than those given by MD when AIREBO-10K and AIREBO-300K are considered.

In case of bending, the MD-to-analytical critical moment ratio varies between 67% and 156%. Overall, the analytical predictions fairly agree with those of Reax-10K (13% difference in average), regardless of the nanotube type (CNT and PhNT). In case of AIREBO-10K and AIREBO-300K, the formula overestimates the critical moments of CNTs (25% difference in average) while it underestimates the critical moments of PhNTs (40% difference in average).

In case of twisting, the MD-to-analytical critical torque ratio varies between 45% and 93%. The predictions are slightly better for the case of Reax-10K (23% difference in average) than for AIREBO-10K and AIREBO-300K (35% difference in average). It is seen that the formula always overestimates the critical torque of CNTs and PhNTs, performing better in case of zig-zag PhNTs and worst for armchair PhNTs.

4. Conclusions

The mechanical properties of armchair and zig-zag PhNTs, with identical diameter to those recently synthetized, were obtained in this work using MD with the Reax forcefield and the AIREBO forcefield. The Reax forcefield allowed an accurate investigation of the bond breaking and rupture mechanisms at 10 K, while AIREBO permitted the obtention of more accurate mechanical properties at 10 K and at 300 K. Both potentials were compared and discussed.

The Reax potential predicts higher stress for identical strains when compared to AIREBO. Thus, the Young's modulus of nanotubes were between 30% and 38% lower with AIREBO, while the tensile strengths were between 48% and 83% lower. The failure strains of CNTs were 2% higher for armchair and 16% lower with zigzag for AIREBO, but with this potential, PhNTs were found to be significantly (between 40 and 58%) lower than with Reax. Compressive strengths were found to be between 22 and 62% higher with AIREBO, while critical strains calculated with AIREBO almost doubled with AIREBO.

With both potentials, the Young's modulus of PhNTs were found to be around 70% lower than that of CNTs, while the tendency in armchair configurations for having higher elasticities is similar in CNTs and PhNTs alike for Reax. For AIREBO zigzag CNTs have higher elasticities than armchair. In both potentials the failure strain was found to be higher for PhNTs than for CNTs, meaning that they can endure longer stretching without breaking apart. PhNTs are much weaker to compression than CNTs but can endure longer strains without buckling, as their critical strains are higher than CNTs (between 29% and 47% with Reax and between 57% and 72% with AIREBO. Temperature degrades the mechanical properties of both CNTs and PhNTs independently of the potential used.

PhNTs revealed a lower bending stiffness (much lower with AIREBO) when compared to CNTs, but it was found that they can tolerate higher angles of bend without bond rupture. The shear modulus and torsional stiffness of PhNTs are much lower than those of CNTs, which means that PhNTs porosity induces an increased flexibility on the nanotubes' sidewalls. On the other hand, the critical angle of twist for PhNTs is slightly higher than for CNTs.

As expected, the Young's modulus, shear modulus, torsional stiffness and bending stiffness of PhNTs are lower those of CNTs. But notably, PhNTs can be compared, in terms of strength, to other carbon allotrope nanotubes such as graphdiynes, but with a more stretchable and flexible carbon lattice. These extra flexibility and extended porosity of PhNTs, makes them very promising candidates for a wide range of applications, such as sensing, ionic transistors, or molecular sieving.

Furthermore, the available and simple elastic buckling formulas developed for (continuum) shells are a direct and straightforward way to evaluate the order of magnitude of the critical stresses, critical moments and critical torques of CNTs and PhNTs, giving a first approach to these values. However, the differences involved between the analytical predictions and the values given by MD are sometimes too high, a fact that must always be accounted for when using continuum formulas.

Declaration of competing interest

The authors declare that they have no known competing financial interests or personal relationships that could have appeared to influence the work reported in this paper.

Data availability

Data will be made available on request.

Acknowledgments

This work was supported by FCT, Portugal, through IDMEC, under LAETA, project UIDB/50022/2020 and by IPC-Institute for Polymers and Composites, Portugal. The first author gratefully acknowledges the financial support given by FCT in the context of CEECINST/00156/2018.

Appendix A. Supplementary data

Supplementary material related to this article can be found online at https://doi.org/10.1016/j.eml.2022.101893.

References

[1] S. Iijima, Helical microtubules of graphitic carbon, Nature 354 (6348) (1991) 56–58, http://dx.doi.org/10.1038/354056A0.

[2] B. Ni, S.B. Sinnott, Chemical functionalization of carbon nanotubes through energetic radical collisions, Phys. Rev. B Conden. Matter Mater. Phys. 61 (24) (2000) R16343–R16346, http://dx.doi.org/10.1103/PHYSREVB.61.R16343.

[3] A.v. Krasheninnikov, K. Nordlund, Stability of irradiation-induced point defects on walls of carbon nanotubes, J. Vac. Sci. Technol. B 20 (2) (2002) 728, http://dx.doi.org/10.1116/1.1463728.

[4] M. Boháčová, et al., Mildly oxidized SWCNT as new potential support membrane material for effective H 2/CO 2 separation, Appl. Mater. Today 15 (2019) 335–342, http://dx.doi.org/10.1016/J.APMT.2019.02.014.

[5] G. Li, et al., Construction of tubular molecule aggregations of graphdiyne for highly efficient field emission, J. Phys. Chem. C 115 (6) (2011) 2611–2615, http://dx.doi.org/10.1021/JP107996F.

[6] A. Pantano, D.M. Parks, M.C. Boyce, Mechanics of deformation of single- and multi-wall carbon nanotubes, J. Mech. Phys. Solids 52 (4) (2004) 789–821, http://dx.doi.org/10.1016/J.JMPS.2003.08.004.

[7] M. Sammalkorpi, A. Krasheninnikov, A. Kuronen, K. Nordlund, K. Kaski, Mechanical properties of carbon nanotubes with vacancies and related defects, Phys. Rev. B 70 (24) (2004) 245416, http://dx.doi.org/10.1103/PhysRevB.70.245416.

[8] B.J. Bucior, D.-L. Chen, J. Liu, J.K. Johnson, Porous Carbon Nanotube Membranes for Separation of H 2/CH 4 and CO 2/CH 4 Mixtures, 2012, http://dx.doi.org/10.1021/jp3098022.

[9] S. Rouhi, Modeling of tensile testing on perfect and defective graphenylene nanotubes using molecular dynamics simulations, Mater. Res. Express 4 (8) (2017) 085012, http://dx.doi.org/10.1088/2053-1591/aa7db2.

[10] J. Xu, S. Meng, Molecular transport across a two-dimensional Nanomesh membrane–graphdiyne, J. Phys. D: Appl. Phys. 53 (49) (2020) http://dx.doi.org/10.1088/1361-6463/ABAFDD.

[11] M. Li, Y. Zhang, Y. Jiang, Y. Zhang, Y. Wang, H. Zhou, Mechanical properties of γ-graphyne nanotubes, RSC Adv. 8 (28) (2018) 15659–15666, http://dx.doi.org/10.1039/C8RA01970C.

[12] S.J. Stuart, A.B. Tutein, J.A. Harrison, A reactive potential for hydrocarbons with intermolecular interactions, J. Chem. Phys. 112 (14) (2000) 6472–6486, http://dx.doi.org/10.1063/1.481208.

[13] S. Rouhi, On the mechanical properties of the graphdiyne nanotubes: a molecular dynamics investigation, Braz. J. Phys. 49 (5) (2019) 654–666, http://dx.doi.org/10.1007/S13538-019-00673-6.

[14] B. Faria, N. Silvestre, J.N.C. Lopes, Strength and fracture of graphyne and graphdiyne nanotubes, Comput. Mater. Sci. 171 (2020) http://dx.doi.org/10.1016/j.commatsci.2019.109233.

[15] K. Chenoweth, A.C.T. van Duin, W.A. Goddard, ReaxFF Reactive Force Field for Molecular Dynamics Simulations of Hydrocarbon Oxidation, 2008, http://dx.doi.org/10.1021/jp709896w.

[16] Z. Sun, et al., Finite phenine nanotubes with periodic vacancy defects, Science (1979) 363 (6423) (2019) 151–155, http://dx.doi.org/10.1126/science.aau5441.

[17] J.Y. Xue, et al., Cyclo-meta-phenylene revisited: Nickel-mediated synthesis, molecular structures, and device applications, J. Org. Chem. 79 (2014) http://dx.doi.org/10.1021/jo501903n.

[18] K. Ikemoto, R. Kobayashi, S. Sato, H. Isobe, Synthesis and bowl-in-bowl assembly of a geodesic phenylene bowl, Angew. Chem. 129 (23) (2017) 6611–6614, http://dx.doi.org/10.1002/ange.201702063.

[19] K. Ikemoto, J. Lin, R. Kobayashi, S. Sato, H. Isobe, Fluctuating carbonaceous networks with a persistent molecular shape: A saddle-shaped geodesic framework of 1, 3, 5-trisubstituted benzene (Phenine), Angew. Chem. Int. Ed. 57 (28) (2018) 8555–8559, http://dx.doi.org/10.1002/ANIE.201803984.

[20] H.T. Yu, M. Yang, W. Zhu, T. Chang, J.W. Jiang, Diameter-dependent polygonal cross section for holey phenine nanotubes, Nanotechnology 31 (8) (2020) http://dx.doi.org/10.1088/1361-6528/AB53A6.

[21] B.D. Jensen, K.E. Wise, G.M. Odegard, The Effect of Time Step, Thermostat, and Strain Rate on ReaxFF Simulations of Mechanical Failure in Diamond, Graphene, and Carbon Nanotube, http://dx.doi.org/10.1002/jcc.23970.

[22] A.P. Thompson, et al., LAMMPS - a flexible simulation tool for particle-based materials modeling at the atomic, meso, and continuum scales, Comput. Phys. Commun. 271 (2022) 108171, http://dx.doi.org/10.1016/J.CPC.2021.108171.

[23] B. Faria, N. Silvestre, J.N.C. Lopes, Mechanical behaviour of carbon nanotubes under combined twisting-bending, Mech. Res. Commun. 73 (2016) http://dx.doi.org/10.1016/j.mechrescom.2016.01.010.

[24] B. Faria, N. Silvestre, J.N. Canongia Lopes, Induced anisotropy of chiral carbon nanotubes under combined tension-twisting, Mech. Mater. 58 (2013) http://dx.doi.org/10.1016/j.mechmat.2012.11.004.

[25] B. Faria, N. Silvestre, J.N. Canongia Lopes, Tension-twisting dependent kinematics of chiral CNTs, Compos. Sci. Technol. 74 (2013) http://dx.doi.org/10.1016/j.compscitech.2012.11.010.

[26] D.J. Evans, B.L. Holian, The Nose–Hoover thermostat, J. Chem. Phys. 83 (8) (1985) 4069–4074, http://dx.doi.org/10.1063/1.449071.

[27] J.A. Zimmerman, W. Iii, J.J. Hoyt, R.E. Jones, P.A. Klein, D.J. Bammann, Calculation of Stress in Atomistic Simulation, 2004, http://dx.doi.org/10.1088/0965-0393/12/4/S03.

[28] D.H. Tsai, The virial theorem and stress calculation in molecular dynamics Articles you may be interested in, J. Chem. Phys. 70 (1979) 1375, http://dx.doi.org/10.1063/1.437577.

[29] S.W. Cranford, M.J. Buehler, Mechanical properties of graphyne, Carbon N.Y. 49 (13) (2011) 4111–4121, http://dx.doi.org/10.1016/J.CARBON.2011.05.024.

[30] Y. Huang, J. Wu, K.C. Hwang, Thickness of graphene and single-wall carbon nanotubes, Phys. Rev. B Conden. Matter Mater. Phys. 74 (24) (2006) 245413, http://dx.doi.org/10.1103/PHYSREVB.74.245413/FIGURES/4/MEDIUM.

[31] R. Rafiee, R.M. Moghadam, On the modeling of carbon nanotubes: A critical review, Composites B 56 (2014) 435–449, http://dx.doi.org/10.1016/J.COMPOSITESB.2013.08.037.

[32] N. Silvestre, On the accuracy of shell models for torsional buckling of carbon nanotubes, Eur. J. Mech. A Solids 32 (2012) 103–108, http://dx.doi.org/10.1016/J.EUROMECHSOL.2011.09.005.

[33] N. Silvestre, C.M. Wang, Y.Y. Zhang, Y. Xiang, Sanders shell model for buckling of single-walled carbon nanotubes with small aspect ratio, Compos. Struct. 93 (7) (2011) 1683–1691, http://dx.doi.org/10.1016/J.COMPSTRUCT.2011.01.004.

[34] N. Silvestre, Length dependence of critical measures in single-walled carbon nanotubes, Int. J. Solids Struct. 45 (4902) (2008) http://dx.doi.org/10.1016/J.IJSOLSTR.2008.04.029, 18–19–4920.

[35] B.I. Yakobson, C.J. Brabec, J. Bernholc, Nanomechanics of carbon tubes: Instabilities beyond linear response, Phys. Rev. Lett. 76 (14) (1996) 2511, http://dx.doi.org/10.1103/PhysRevLett.76.2511.